



UNIVERSITY OF CLAUDE BERNARD LYON 1  
Polytech Lyon

---

**Estimation of Image-Derived Arterial Input Function in  
Brain PET Imaging:  
Application to Modeling PET Dynamics of Glucose  
Metabolism in Patients with Impaired Consciousness**

---

By SEPAND ALI MADAD SOLTANI

Master's Thesis Report

Supervised by INÉS MÉRIDA and NICOLAS COSTES

Academic Advisor: KEVIN TSE VE KOON

November 2024 - January 2025



# Abstract

**Keywords:** PET, Image-Derived, ...

# Contents

<b>1</b>	<b>Introduction</b>	<b>1</b>
1.1	Positron Emission Tomography . . . . .	1
1.2	Compartmental Model . . . . .	2
1.3	Input Function . . . . .	3
1.3.1	Arterial Input Function . . . . .	3
1.3.2	Image Derived Input Function . . . . .	3
<b>2</b>	<b>Materials and Methods</b>	<b>5</b>
2.1	Dataset Description . . . . .	5
2.2	Carotid Segmentation . . . . .	5
2.3	Partial Volume Correction . . . . .	6
2.3.1	Geometric Transfer Matrix . . . . .	6
2.3.2	Bayesian Geometric Transfer Matrix . . . . .	7
2.4	Quantification . . . . .	7
2.5	Evaluation . . . . .	8
2.6	Implementation . . . . .	9
<b>3</b>	<b>Results</b>	<b>10</b>
3.1	Segmentation . . . . .	10
3.2	IDIF . . . . .	10
<b>4</b>	<b>Discussion</b>	<b>14</b>
<b>5</b>	<b>Conclusion</b>	<b>15</b>
	<b>References</b>	<b>16</b>

# Introduction

## 1.1 Positron Emission Tomography

Positron Emission Tomography (PET) is a functional imaging technique widely used in clinical and research settings to monitor physiological processes. In PET, a biologically active molecule is labeled with a positron-emitting radioisotope, serving as a radiotracer, and then injected into the body. As the radiotracer accumulates in target tissues, its radioactive decay produces positrons, which interact with electrons to emit pairs of gamma photons in nearly opposite directions. These photons are detected by the PET scanner, and image reconstruction algorithms generate a three-dimensional representation of the tracer distribution. This imaging modality allows for the investigation of metabolic changes, receptor binding, and other biochemical processes, providing invaluable information in oncology, neurology, cardiology, and other fields.

There are two main methods for acquiring PET images: static imaging and dynamic imaging. Static PET involves acquiring a single scan after the radiotracer injection. This single snapshot offers a powerful yet simplified view of tracer distribution. The common quantification metric in static imaging is the Standardized Uptake Value (SUV), which normalizes tissue uptake by the injected dose and patient weight, allowing for a semi-quantitative comparison of tracer accumulation across different tissues or over time [TODO]. Due to its simplicity, static PET is widely used in clinical settings; however, it also has limitations. Because it reflects only one time point, the SUV cannot capture the temporal dynamics of tracer uptake and clearance, and various physiological factors may influence its measurements, thereby reducing its accuracy.

Dynamic PET imaging provides a more comprehensive view of radiotracer kinetics by acquiring a series of images over a period ranging from a few minutes to more than an hour, depending on the tracer type. Instead of a single snapshot, dynamic imaging produces time-activity curves (TACs) that illustrate how tracer concentration in each tissue changes throughout the scanning period. This approach enables the measurement of physiological parameters such as the tracer rate of influx ( $K_1$ ), volume of distribution ( $V_T$ ), and the rates of phosphorylation and dephosphorylation.

## 1.2 Compartmental Model

To quantify these parameters, kinetic modeling is employed. Various graphical models (e.g., the Logan [TODO] and Patlak [TODO] methods) have been proposed; however, compartmental modeling is the most popular and is considered the most accurate approach in kinetic modeling. In compartmental modeling, the distribution and kinetics of a radiotracer are described by dividing the system into distinct compartments, each representing a pool of tracer that behaves uniformly. Interactions between compartments can be unidirectional or bidirectional, meaning the tracer may either move in and out or only enter a compartment.

Here, we focus on the two-tissue compartment model (2TCM), also known as the three-compartment model in series mode when using FDG as the tracer. This model comprises one tissue compartment for the free tracer,  $C_F(t)$ , and another for the receptor-bound tracer,  $C_B(t)$ , in addition to an external compartment representing the tracer concentration in the plasma or blood, denoted as the input function  $C_P(t)$ .

The tracer kinetics are governed by a series of first-order differential equations, in which the exchange rates between the compartments are considered constant:

$$\frac{dC_F(t)}{dt} = K_1 C_P(t) - (k_2 + k_3)C_F(t) + k_4 C_B(t), \quad (1.1)$$

$$\frac{dC_B(t)}{dt} = k_3 C_F(t) - k_4 C_B(t), \quad (1.2)$$

where  $K_1$ ,  $k_2$ ,  $k_3$ , and  $k_4$  are the constant rate parameters.

It is generally assumed that once FDG is phosphorylated (i.e., bound), there is little to no dephosphorylation back to the free (unbound) compartment. Therefore, we can set  $k_4 = 0$  [TODO]. This assumption leads to the irreversible two-tissue compartment model. Thus, Equations (1.1) and (1.2) simplify to

$$\frac{dC_F(t)}{dt} = K_1 C_P(t) - (k_2 + k_3)C_F(t), \quad (1.3)$$

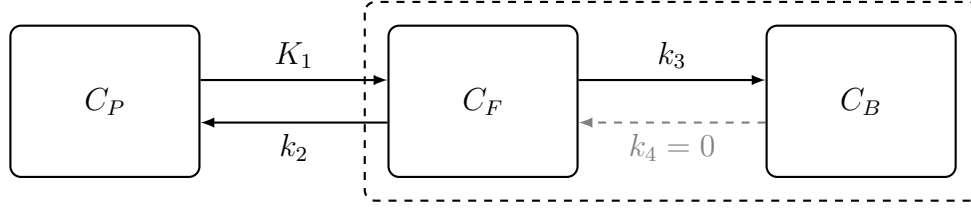
$$\frac{dC_B(t)}{dt} = k_3 C_F(t). \quad (1.4)$$

The total concentration measured by PET,  $C_T(t)$ , is given by

$$C_T(t) = C_F(t) + C_B(t) + C_P(t). \quad (1.5)$$

The parameters  $K_1$ ,  $k_2$ , and  $k_3$  can be estimated by fitting the model to the measured PET time-activity curves (TACs), using  $C_P(t)$  as the input function. Consequently, the influx rate (trapping rate) of FDG in the tissue,  $K_i$ , can be derived as

$$K_i = \frac{K_1 \times k_3}{k_2 + k_3}. \quad (1.6)$$



**Figure 1.1:** Schematic of the irreversible two-tissue compartment model (2TCM)

FDG is an analog of glucose, not glucose itself. To convert the FDG trapping rate into the actual rate of glucose metabolism, both the glucose concentration and the lumped constant must be taken into account.

$$\text{MR}_{glu} \text{ (}\mu\text{mol/min/100g)} = \frac{[C]}{LC} \cdot K_i. \quad (1.7)$$

Here,  $\text{MR}_{glu}$  represents the metabolic rate of glucose,  $[C]$  denotes the glucose concentration, and  $LC$  is the lumped constant.

## 1.3 Input Function

### 1.3.1 Arterial Input Function

The arterial input function (AIF) is considered the gold standard for obtaining the input function. It is determined by inserting an arterial catheter into the patient and continuously drawing blood samples to measure the radiotracer concentration, thereby obtaining the blood time-activity curve (TAC) used in the quantification model. However, this procedure is invasive and can cause discomfort, potentially discouraging patients from undergoing future examinations. Furthermore, this method is labor-intensive and requires trained personnel to manage both the patient and the measurement devices.

### 1.3.2 Image Derived Input Function

The image-derived input function (IDIF) has been proposed as a non-invasive alternative for obtaining the input function. IDIF techniques typically involve identifying vascular structures or regions with high blood pool activity within the imaging field and extracting the input function directly from the PET images. In brain PET imaging, the carotid arteries are the largest vessels present in the limited field of view (FOV) and have a diameter of approximately 5 mm, which is comparable to the typical spatial resolution of PET. Therefore, directly extracting the carotids from PET images is impractical due to the limited resolution and the strong partial volume effects (PVE) present.

With the emergence of hybrid PET/MRI machines, simultaneous acquisition of functional and anatomical data has become possible, with MRI providing high-resolution soft

tissue contrast while PET captures metabolic activity. Time-of-flight (TOF) MR angiography (MRA) offers high contrast in arteries, enabling accurate segmentation of the carotids. However, even with precise segmentation, the input function obtained by directly applying the mask to the PET image suffers from partial volume effects and requires appropriate correction.

With the emergence of hybrid PET/MRI machines, it has become feasible to acquire both functional and anatomical data simultaneously. MRI provides high-resolution soft tissue contrast, while PET captures metabolic activity. For instance, time-of-flight (TOF) MR angiography (MRA) delivers excellent arterial contrast, which allows for accurate segmentation of vascular structures such as the carotid arteries. However, even with a high-resolution anatomical guidance, directly applying the segmented arterial mask to the PET images introduces challenges. In particular, the limited spatial resolution of PET can lead to partial volume effects, resulting in inaccuracies in the derived input function. Consequently, additional correction techniques are required to mitigate these effects and ensure reliable quantification.


[TODO] include more bibliography here.

Irace et al. [1] proposed a method for IDIF estimation by performing MRA-driven carotid segmentation and using a Bayesian framework for incorporating prior knowledge into a geometric transfer matrix method—a classical partial volume correction technique. The aim here was to improve on this method and increase accuracy.



# Materials and Methods

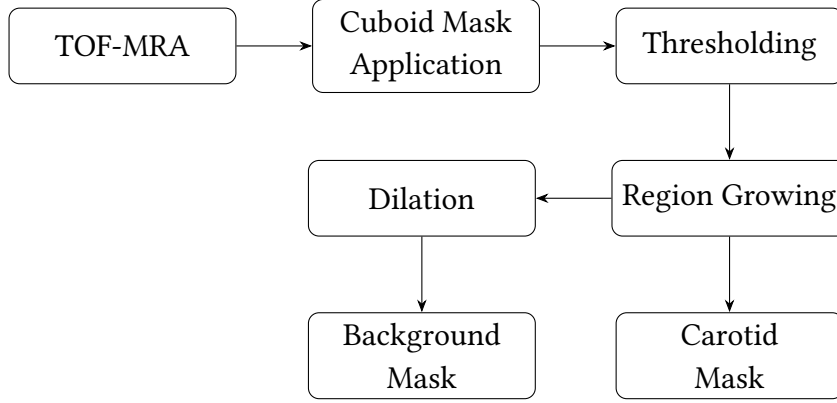
## 2.1 Dataset Description

We utilized a dataset comprising 56 comatose patients, aged between X and Y years. For each patient, dynamic PET imaging was performed over a 90-minute period using  $^{18}\text{F}$ FDG as the tracer. In addition, arterial blood sampling and TOF-MRA images were acquired during the same session. 

## 2.2 Carotid Segmentation

Since vessels appear as hypersignal in TOF-MRA, a high-intensity thresholding technique was employed. First, a threshold value was computed by selecting all nonzero intensity values and then determining the intensity level at the  $(1 - 0.003)$  quantile (i.e., the 99.7th percentile) of these intensities. Only voxels exceeding this threshold and located outside the brain mask were retained. Next, a region-growing step was applied to refine the initial selection, ensuring that continuous vascular structures were captured as the final carotid mask.

In addition to arteries, venous structures and possible brain lesions may also appear as hypersignal and might be selected by the algorithm. To exclude them, a cuboid mask was defined in a reference image covering the neck area up to the bottom of the brain, where the carotid is most likely to appear. The MRA image was first registered to the reference image using an affine registration technique (FSL FLIRT). Using the obtained affine matrix, the cuboid mask was first transformed and then applied to the MRA image before thresholding step to ensure the mentioned unwanted tissues will not effect the intensity histograms and do not get selected as carotid.



**Figure 2.1:** Carotid and background mask segmentation pipeline

## 2.3 Partial Volume Correction

### 2.3.1 Geometric Transfer Matrix

Direct quantification with the IDIF extracted from the MRI mask of the carotid is impractical due to the strong Partial Volume Effects (PVE) in PET images. This however can be corrected by the use of the Geometric Transfer Matrix (GTM) method. This method considers the observed TAC to be the linear combination of the true real value and the other effecting regions. Here we define two regions, the carotid and the background mask which was generated by dilating the carotid mask by 5 pixels and subtracting the voxels corresponding to the carotid mask.

$$\underbrace{\begin{bmatrix} T_c \\ T_{bg} \end{bmatrix}}_{\text{Observed}} = \underbrace{\begin{bmatrix} \omega_{c \rightarrow c} & \omega_{bg \rightarrow c} \\ \omega_{c \rightarrow bg} & \omega_{bg \rightarrow bg} \end{bmatrix}}_{\text{GTM}} \cdot \underbrace{\begin{bmatrix} T_{IF} \\ T_{tissue} \end{bmatrix}}_{\text{Unknown}}, \quad (2.1)$$

where  $\omega_{n \rightarrow m}$  is the spill coefficient of region  $n$  onto region  $m$ , which is obtained by convolving the binary mask of region  $n$  with the system's point spread function and integrating the resulting intensity over region  $m$ , normalized by the total signal in region  $m$ . where

$$\omega_{n \rightarrow m} = \frac{\int_{\Omega_m} (h * \chi_n)(\mathbf{r}) d\mathbf{r}}{\int_{\Omega_m} (h * \chi_m)(\mathbf{r}) d\mathbf{r}}, \quad (2.2)$$

with  $\chi_n$  and  $\chi_m$  denoting the binary masks of regions  $n$  and  $m$ , respectively,  $h$  the system's point spread function, and  $\Omega_m$  the spatial domain of region  $m$ .

$T_c$  and  $T_{bg}$  are respectively the observed carotid and background TACs and  $T_{IF}$  and  $T_{tissue}$  are the real unknown TACs of the carotid (the input function) and the background tissue.

By inverting the GTM, this system of equations can be easily solved. However, the GTM

being a low rank matrix makes the inversion sensitive to noise and biased on small regions such as the carotid.

### 2.3.2 Bayesian Geometric Transfer Matrix

To overcome challenges posed to GTM method, we utilized a Bayesian framework that jointly estimates the input function and tissue kinetics. For each subject,  $T_{IF}$  is modeled as a linear combination of a population mean and its principal components. These components are derived by performing principal component analysis (PCA) on a set of AIFs collected from the population. Specifically, for each subject, a subset of 10 random subjects is selected from the dataset—excluding the subject under study—to construct the PCA model.

$$T_{IF}(t) = \mu(t) + \theta_1 v_1(t) + \theta_2 v_2(t) + \theta_3 v_3(t), \quad (2.3)$$

where  $\mu(t)$  is the population mean AIF,  $v_i(t)$  are the principal components obtained from PCA, and  $\theta_i$  are the subject-specific weighting coefficients.

The background TAC is then generated by convolving this modeled input function with an impulse response function (IRF) defined by a two-tissue compartment model [2].

$$T_{bg}(t) = T_{IF}(t) \otimes IRF(t; K_1, k_2, k_3), \quad (2.4)$$

where  $K_1$ ,  $k_2$ , and  $k_3$  are kinetic parameters of the two-tissue compartment and  $IRF$  is

$$IRF(t) = a_0 e^{-(k_2+k_3)t} + a_1 \text{ with } a_0 = \frac{K_1 k_2}{k_2 + k_3}, a_1 = \frac{K_1 k_3}{k_2 + k_3}. \quad (2.5)$$

Parameter estimation is performed using a Metropolis-within-Gibbs Markov Chain Monte Carlo (MCMC) sampler, which explores the posterior distribution of both the kinetic parameters and the PCA coefficients. In the Bayesian framework [1], all model parameters are collected into the vector  $\Theta$ . The posterior distribution of  $\Theta$  given the observed data  $\mathcal{D}$  is expressed as

$$p(\Theta | \mathcal{D}) \propto p(\mathcal{D} | \Theta) \pi(\Theta), \quad (2.6)$$

where  $p(\mathcal{D} | \Theta)$  is the likelihood function and  $\pi(\Theta)$  is the prior distribution over the parameters  $\Theta = (\theta_1, \theta_2, \theta_3, K_1, k_2, k_3)$ . The maximum a posteriori (MAP) estimate of  $\Theta$  is given by:

$$\hat{\Theta} = \arg \max_{\Theta} \{ \ln p(\mathcal{D} | \Theta) + \ln \pi(\Theta) \}. \quad (2.7)$$

## 2.4 Quantification

To accurately evaluate the performance of the estimated IDIF against the gold standard AIF, we performed absolute quantification using an irreversible two-tissue compartment

model (2TCM) via non-linear fitting with the `fitk3` program from the TPCCLIB library developed at the Turku PET Centre [3]—applying the model fitting once with the IDIF and once with the AIF as the input function. The brain was segmented into regions of interest (ROI) based on the Hammersmith brain atlas [TODO], and time-activity curves (TACs) were generated by averaging voxels over each ROI at every time point. The regional influx rate ( $K_i$ ) was then calculated, from which the corresponding  $MR_{glu}$  values were derived.

## 2.5 Evaluation

The performance of the proposed IDIF estimation was first evaluated by computing the mean absolute error between the cumulative area under the curve (cAUC) of the estimated IDIF and the *true* AIF. cAUC was considered to be a more suitable metric since it provides an integrated measure of tracer exposure over time and is less sensitive to local fluctuations or noise in the curve compared to the directly comparing the TACs.

$$cAUC(t) = \int_0^t IF(\tau) d\tau, \quad (2.8)$$

where  $IF$  is the input function.

However, because the cAUC error does not fully capture the impact of IDIF deviations on kinetic parameters, absolute quantification was also performed to assess overall performance more accurately. The quantification program was run using both the IDIF and AIF as input functions, and the regional metabolic rate of glucose was compared between the two methods.

The mean absolute percentage error (MAPE) of the  $MR_{glu}$  in each ROI was calculated and then averaged across the entire dataset:

$$\text{Average MAPE}(MR_{glu}) = \frac{100\%}{N} \sum_{i=1}^N \left( \frac{1}{N_{ROI}} \sum_{j=1}^{N_{ROI}} \left| \frac{MR_{glu,ij}^{IDIF} - MR_{glu,ij}^{AIF}}{MR_{glu,ij}^{AIF}} \right| \right). \quad (2.9)$$

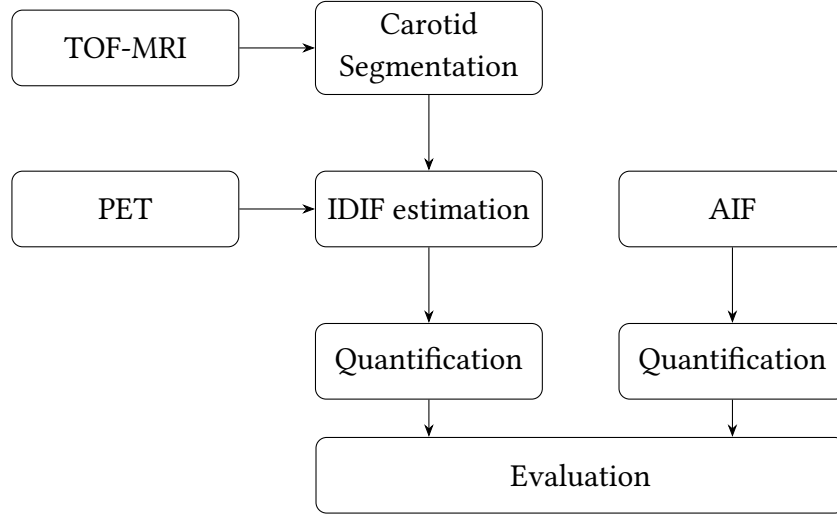
Additionally, linear least-squares regression was performed between the regional  $MR_{glu}$  obtained by quantification with using AIF and IDIF for each subject. The coefficient of determination ( $R^2$ ) and the regression slope ( $S$ ) were obtained for each subject. The mean absolute errors (MAE) of these metrics across the dataset are given by

$$MAE(R^2) = \frac{1}{N} \sum_{i=1}^N |R_i^2 - 1| \quad (2.10)$$

and

$$MAE(S) = \frac{1}{N} \sum_{i=1}^N |S_i - 1|, \quad (2.11)$$

where  $R_i^2$  and  $S_i$  denote the coefficient of determination and the regression slope for subject  $i$ , respectively.



**Figure 2.2:** The IDIF estimation and evaluation pipeline

## 2.6 Implementation

The code was primarily implemented in Python, with some auxiliary components in Bash scripts. The underlying algorithm and implementation was originally developed by Irace et al. [1]. Building on this foundation, a number of improvements and additions were introduced to the code and the algorithm.

In the original carotid segmentation algorithm, the TOF-MRA image was smoothed to reduce noise. The purpose of this smoothing step was to attenuate noise; however, because carotids inherently exhibit high-frequency spatial features, the smoothing inadvertently blurred these critical details, ultimately reducing the accuracy of the segmentation. Hence, this step was removed.

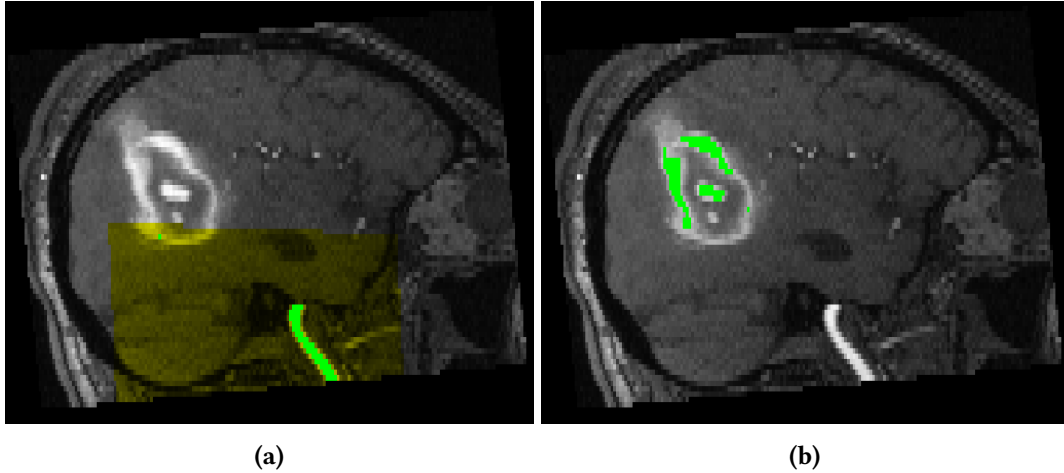
In the adaptive thresholding step, all voxels, including those with zero intensity were originally included. This led to a significant imbalance in the intensity histograms, making the thresholding highly susceptible to variations in the number of slices and the effects of zero padding in the TOF-MRA image. Limiting to only nonzero voxels resulted in an immediate improvement in the final segmentation. Despite these improvements, some non-carotid tissues were inadvertently selected by the algorithm, hence the cuboid mask mentioned in Section 2.2 was introduced.

Significant improvements have been made to the overall code quality and performance. These include major bug fixes, streamlining the pipeline, multi-processing support, and the integration of evaluation metrics for individual subjects as well as for overall dataset performance.

# Results

## 3.1 Segmentation

The measures described in Section 2.2 significantly improved carotid segmentation by effectively excluding brain lesions and undesired venous structures. As illustrated in Figure 3.1, the cuboid mask plays a crucial role in this process. Because no ground truth segmentation is available, visual inspection was used to evaluate the results, which showed that lesions and venous structures were rarely selected by the algorithm. However, the algorithm was sometimes overly conservative. In some instances, even when no non-carotid tissues were selected, parts of the carotid were inadvertently excluded.



**Figure 3.1:** Comparison of carotid segmentation (green) with (a) and without (b) a cuboid mask (yellow). In the absence of the cuboid mask, the segmentation algorithm fails to capture the carotid and instead incorrectly identifies the brain lesion

## 3.2 IDIF

IDIF estimation was performed using both the Bayesian GTM (BGTM) and the conventional GTM PVC method. The average mean absolute error (MAE) of the cumulative area under the curve (cAUC) across the dataset was 14,202 for BGTM and 33,764 for GTM.

ROI-based quantification was carried out using both IDIF methods, with BGTm yielding significantly better performance. Specifically, the BGTm and GTm methods achieved an average  $MR_{glu}$  mean absolute percentage error (MAPE) of 14.1% and 33%, respectively, and an average  $MR_{glu}$  mean absolute error (MAE) of 1.42 and 3.5. In addition, the MAE for the coefficient of determination ( $R^2$ ) and the regression slope ( $S$ ) were 0.004 and 0.14 for BGTm, compared to 0.030 and 0.304 for GTm, respectively.

Metric	BGTm		GTm	
	$\mu$	$\sigma$	$\mu$	$\sigma$
cAUC MAE	14,202	9,190	33,764	21,212
$MR_{glu}$ MAPE (%)	<b>14.1</b>	<b>10.1</b>	33.0	31.5
$MR_{glu}$ MAE	1.42	1.07	3.50	3.38
$R^2$ Error	0.004	0.006	0.030	0.132
Slope Error	0.14	0.109	0.304	0.230

Table 3.1: Summary of performance metrics for BGTm and GTm methods.

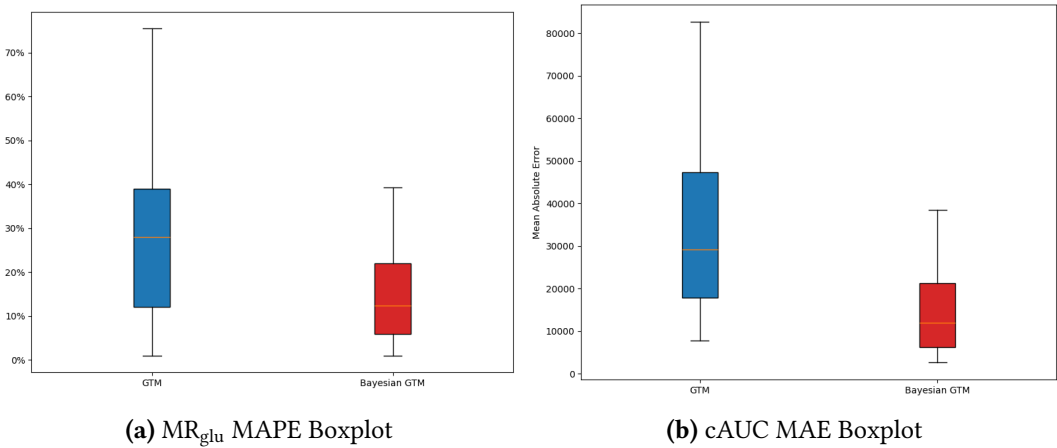

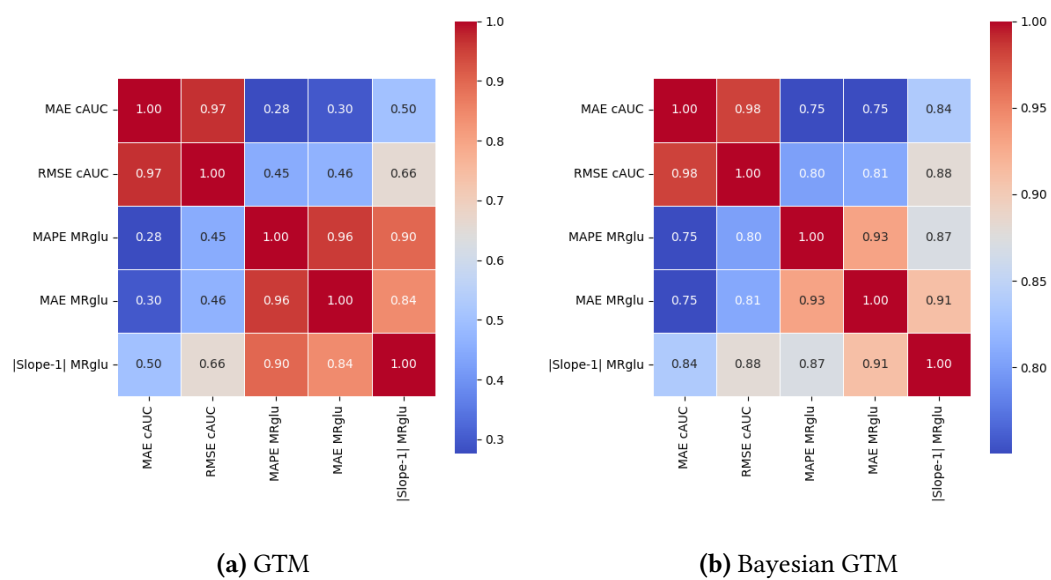


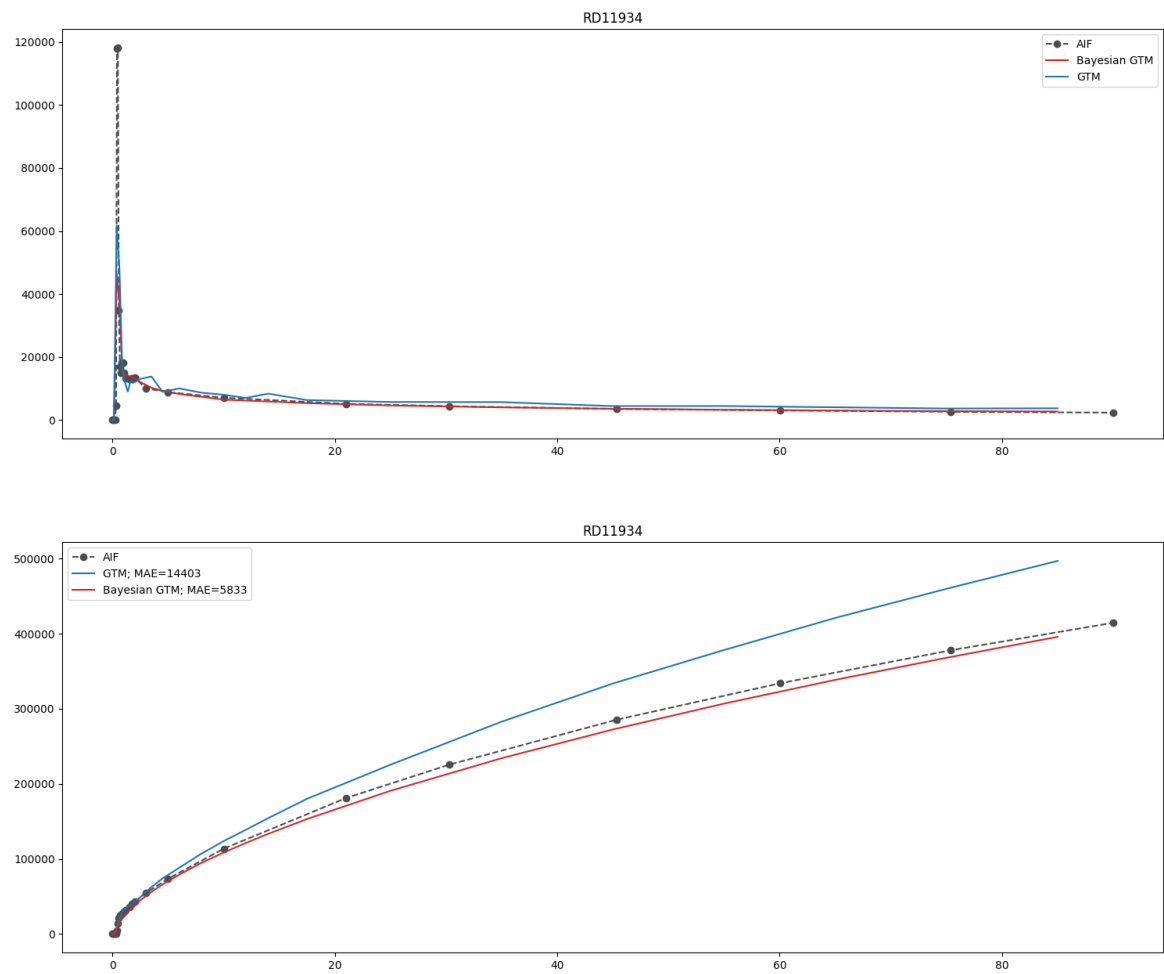
Figure 3.2: Boxplot of curve and quantification errors

As illustrated in Figure ??, there is a strong correlation between the MAE of the cAUC error and the quantification errors showing cAUC can be a good intermediate metric. 



**Figure 3.3:** Correlation matrix of different metrics for Bayesian GTM and GTM methods





**Figure 3.4:** Comparison of the IFs (Top) and Cumulative AUC curves (Bottom) for a specific subject

# Discussion

# Conclusion

# References

- [1] Zacharie Irace et al. “Bayesian partial volume correction for image derived input function”. In: *JOURNAL OF CEREBRAL BLOOD FLOW AND METABOLISM*. Vol. 41. 1\_ SUPPL. SAGE PUBLICATIONS INC 2455 TELLER RD, THOUSAND OAKS, CA 91320 USA. 2021, pp. 229–229.
- [2] Camille Juvie. “Estimation de la fonction d’entrée en tomographie par émission de positons dynamique : application au fluorodesoxyglucose”. Theses. Université Paris Sud - Paris XI, Dec. 2013.
- [3] Vesa Oikonen et al. *TPCCLIB*. Version 0.6.20. Retrieved on 2nd February 2025. Turku PET Centre, University of Turku, 2018. URL: <https://gitlab.utu.fi/vesoik/tpcclib>.